

## Article

# First Principles Study of the Structure–Performance Relation of Pristine $W_{n+1}C_n$ and Oxygen-Functionalized $W_{n+1}C_nO_2$ MXenes as Cathode Catalysts for Li-O<sub>2</sub> Batteries

Liwei Zhu , Jiajun Wang , Jie Liu, Ruxin Wang, Meixin Lin, Tao Wang, Yuchao Zhen, Jing Xu \* and Lianming Zhao \* 

School of Materials Science and Engineering, China University of Petroleum (East China), Qingdao 266580, China; 2114010430@s.upc.edu.cn (L.Z.); lw13255323168@163.com (J.W.); 2114011202@s.upc.edu.cn (J.L.); 2214010605@s.upc.edu.cn (R.W.); linmeixin5683@163.com (M.L.); wangtaoqwas@163.com (T.W.); 15688469531@163.com (Y.Z.)

\* Correspondence: xujing@upc.edu.cn (J.X.); lmzhao@upc.edu.cn (L.Z.)

**Abstract:** Li-O<sub>2</sub> batteries are considered a highly promising energy storage solution. However, their practical implementation is hindered by the sluggish kinetics of the oxygen reduction (ORR) and oxygen evolution (OER) reactions at cathodes during discharging and charging, respectively. In this work, we investigated the catalytic performance of  $W_{n+1}C_n$  and  $W_{n+1}C_nO_2$  MXenes ( $n = 1, 2,$  and  $3$ ) as cathodes for Li-O<sub>2</sub> batteries using first principles calculations. Both  $W_{n+1}C_n$  and  $W_{n+1}C_nO_2$  MXenes show high conductivity, and their conductivity is further enhanced with increasing atomic layers, as reflected by the elevated density of states at the Fermi level. The oxygen functionalization can change the electronic properties of WC MXenes from the electrophilic W surface of  $W_{n+1}C_n$  to the nucleophilic O surface of  $W_{n+1}C_nO_2$ , which is beneficial for the activation of the Li-O bond, and thus promotes the Li<sup>+</sup> deintercalation during the charge–discharge process. On both  $W_{n+1}C_n$  and  $W_{n+1}C_nO_2$ , the rate-determining step (RDS) of ORR is the formation of the (Li<sub>2</sub>O)<sub>2</sub>\* product, while the RDS of OER is the LiO<sub>2</sub>\* decomposition. The overpotentials of ORR and OER are positively linearly correlated with the adsorption energy of the RDS Li<sub>x</sub>O<sub>2</sub>\* intermediates. By lowering the energy band center, the oxygen functionalization and increasing atomic layers can effectively reduce the adsorption strength of the Li<sub>x</sub>O<sub>2</sub>\* intermediates, thereby reducing the ORR and OER overpotentials. The  $W_4C_3O_2$  MXene shows immense potential as a cathode catalyst for Li-O<sub>2</sub> batteries due to its outstanding conductivity and super-low ORR, OER, and total overpotentials (0.25, 0.38, and 0.63 V).

**Keywords:** density functional theory; electrocatalysis; oxygen reduction reaction; oxygen evolution reaction



**Citation:** Zhu, L.; Wang, J.; Liu, J.; Wang, R.; Lin, M.; Wang, T.; Zhen, Y.; Xu, J.; Zhao, L. First Principles Study of the Structure–Performance Relation of Pristine  $W_{n+1}C_n$  and Oxygen-Functionalized  $W_{n+1}C_nO_2$  MXenes as Cathode Catalysts for Li-O<sub>2</sub> Batteries. *Nanomaterials* **2024**, *14*, 666. <https://doi.org/10.3390/nano14080666>

Academic Editor: Carlos Miguel Costa

Received: 18 March 2024  
Revised: 6 April 2024  
Accepted: 9 April 2024  
Published: 11 April 2024



**Copyright:** © 2024 by the authors. Licensee MDPI, Basel, Switzerland. This article is an open access article distributed under the terms and conditions of the Creative Commons Attribution (CC BY) license (<https://creativecommons.org/licenses/by/4.0/>).

## 1. Introduction

Energy conversion and storage systems have become a critical component of the future energy sector as global energy demand continues to grow and energy transformation accelerates. Among these systems, Li-O<sub>2</sub> batteries are considered one of the most promising solutions for energy storage due to their high energy density (up to 3500 Wh·kg<sup>−1</sup>), long lifespan, and environmental friendliness [1]. Li-O<sub>2</sub> batteries typically are composed of lithium metal anodes, oxygen cathodes, and non-aqueous Li<sup>+</sup> conductive electrolytes [2]. During discharge, atmospheric oxygen reacts with (Li<sup>+</sup> + e<sup>−</sup>) pairs to form (Li<sub>2</sub>O)<sub>2</sub>, which undergoes an oxygen reduction reaction (ORR) on the cathode:



Upon charging, (Li<sub>2</sub>O)<sub>2</sub> is converted back to (Li<sup>+</sup> + e<sup>−</sup>) and O<sub>2</sub>. Therefore, the oxygen evolution reaction (OER) takes place at the cathode [3]. However, the sluggish kinetics of ORR and OER at the cathode lead to increased charge and discharge overpotentials,

limited discharge capacity, and inadequate cycling performance of Li-O<sub>2</sub> batteries, thereby limiting their practical applicability [4]. Furthermore, due to the poor conductivity of the discharge product Li<sub>2</sub>O<sub>2</sub>, its decomposition during charging requires a significant overpotential, resulting in the decomposition of the solvent at high voltage. Additionally, other components in the air, such as CO<sub>2</sub> and H<sub>2</sub>O, may react with Li<sub>2</sub>O<sub>2</sub> to form by-products, such as Li<sub>2</sub>CO<sub>3</sub> and LiOH, which are more difficult to decompose. Finally, the battery reaches a fault state [5,6]. Consequently, the development and synthesis of efficient cathode catalysts play a pivotal role in enhancing the performance of Li-O<sub>2</sub> batteries. To date, several categories of catalyst materials have been employed in Li-O<sub>2</sub> batteries, including noble metals and their alloys (Pt [7] and Pt-Au alloys [8]), functional carbon materials (graphene [9] and carbon nanotube [10]), transition metal oxides (Mn<sub>3</sub>O<sub>4</sub> [11] and Co<sub>3</sub>O<sub>4</sub> [12]), transition metal carbides/nitrides (Mo<sub>2</sub>C [13] and MoN [1]), metal-organic frameworks (Ru-MOF-C [14] and Tz-Mg-MOF-74 [15]), and other composite structure electrocatalysts [16,17].

In recent years, MXenes have attracted considerable attention in the field of electrocatalysis due to their unique properties as two-dimensional (2D) layered nitride or carbide materials, including low resistivity, fast ion transport, and tunable interlayer structure [18]. MXenes are typically fabricated utilizing three layers of the MAX phase as a precursor, followed by etching the A layer via various techniques and modifying functional groups on the surface. The general formula for MAX phases is M<sub>n+1</sub>AX<sub>n</sub>. The synthesized MXenes can be represented as M<sub>n+1</sub>X<sub>n</sub>T<sub>x</sub>, where M is a transition metal (such as Cr, Ti, Mn, Mo, or W), A is usually a group 13 or 14 elements (such as Al, Si, Ga, or Ge), X is C or N, and T represents the end of surface (such as O, F, or OH). Nowadays, various MXenes have been used in Li-O<sub>2</sub> batteries [19] and supercapacitors [20]. For example, Xu et al. reported that the O-terminated V<sub>2</sub>C MXene (V<sub>2</sub>CO<sub>2</sub>) can significantly reduce battery overpotential to 0.75 V, increase capacity to 8577 mAh g<sup>-1</sup> at 100 mA g<sup>-1</sup>, and improve durability up to 302 cycles for Li-O<sub>2</sub> batteries. The electrocatalytic activity of V<sub>2</sub>CO<sub>2</sub> is enhanced by improving the affinity for the substrate with Li<sub>2</sub>O<sub>2</sub> through O-termination. Moreover, the unique 2D V<sub>2</sub>CO<sub>2</sub> structure exhibits remarkable conductivity and excellent mass transfer performance during battery operation, thereby effectively optimizing the dynamics of Li-O<sub>2</sub> batteries [18]. The Nb<sub>2</sub>C MXene nano-sheets with uniform O-terminal surfaces were fabricated as a high-rate cathode for Li-O<sub>2</sub> batteries by Li et al. [21]. This catalyst exhibits a large capacity of 19785.5 mAh g<sup>-1</sup> and a high-rate stability of 130 cycles at 200 mA g<sup>-1</sup> and 3 A g<sup>-1</sup> [21]. Density functional theory (DFT) calculations indicate that the O-terminated Nb<sub>2</sub>C MXene can enhance its affinity with LiO<sub>2</sub> and Li<sub>2</sub>O<sub>2</sub>, facilitating spatial orientation accumulation and stable decomposition of discharge products [21]. These findings highlight the significant potential of MXenes in Li-O<sub>2</sub> batteries. However, further research is needed to elucidate the relationship between MXene structure and activity in Li-O<sub>2</sub> batteries, especially regarding the influence of surface functional groups and the number of atomic layers of M<sub>n+1</sub>X<sub>n</sub>T<sub>x</sub> MXene on catalytic performance.

In light of these formidable challenges, we systematically investigate the catalytic performance of WC-MXenes (i.e., W<sub>n+1</sub>C<sub>n</sub> and W<sub>n+1</sub>C<sub>n</sub>O<sub>2</sub>, n = 1, 2, and 3) as cathode materials for Li-O<sub>2</sub> batteries through first principles calculations. The WC-MXenes were selected for the following benefits: (a) W-based materials exhibit excellent mechanical strength, outstanding chemical stability, and high tolerance to acidic environments, and are naturally abundant and environmentally friendly [22,23]. (b) The W<sub>x</sub>C<sub>y</sub> materials have been proven Pt-like catalytic features in many electrochemical reactions, such as ORR and OER [24]. (c) WC MXenes have a metallic nature, high charge capacity, and low Li<sup>+</sup> diffusion barrier, facilitating the rapid deintercalation of Li<sup>+</sup> during the charge-discharge process [25–27].

Herein, the electrochemical catalytic models of the WC MXene cathode were established to simulate OER and ORR during the charge-discharge process. The relationship between structure and catalytic performance of WC MXenes was revealed. In particular, the effects of surface oxygen functionalization and atomic layer number on the electronic

structure of WC MXenes were explored to modulate the ORR and OER activities. We focused solely on the intrinsic properties of the electrocatalysts. External factors such as discharge product morphology, electrolyte decomposition, side reactions with CO<sub>2</sub> and H<sub>2</sub>O, lithium metal corrosion, and oxygen electrode polarization were not considered in this work. Initially, the geometric and electronic structures of pristine and functionalized WC MXenes were investigated, revealing that both pristine W<sub>n+1</sub>C<sub>n</sub> and O-functionalized W<sub>n+1</sub>C<sub>n</sub>O<sub>2</sub> (n = 1, 2, and 3) show excellent electrical conductivity. Furthermore, the influence of atomic layer number and oxygen functional groups on the electronic properties and catalytic activity of WC MXenes was examined. Then, the formation and reversible decomposition of Li<sub>x</sub>O<sub>2</sub> (x = 1, 2, and 4) were simulated during charge–discharge processes. Finally, the overpotentials of WC MXenes were quantitatively calculated to evaluate their catalytic performance for Li–O<sub>2</sub> batteries. Our study demonstrates that oxygen functionalization can convert the electrophilic W surface of W<sub>n+1</sub>C<sub>n</sub> to the nucleophilic O surface of W<sub>n+1</sub>C<sub>n</sub>O<sub>2</sub>, promoting the deintercalation of Li<sup>+</sup> during the charge–discharge process. The ORR and OER overpotentials are positively linearly correlated with the adsorption energy of the Li<sub>x</sub>O<sub>2</sub>\* intermediates. Surface oxygen functionalization and increasing atomic layers can weaken the Li<sub>x</sub>O<sub>2</sub> adsorption by lowering the energy band center of WC MXenes, thereby reducing the ORR/OER overpotentials. Notably, the W<sub>4</sub>C<sub>3</sub>O<sub>2</sub> MXene shows the superior catalytic performance, characterized by high conductivity and ultra-low ORR, OER, and total overpotentials (0.25, 0.38, and 0.63 V). This study bridges the gap left by WC MXenes as cathode catalysts for Li–O<sub>2</sub> batteries and enriches the research of the MXene family in Li–O<sub>2</sub> batteries.

## 2. Details of the Calculation

In this study, all spin-unrestricted DFT calculations were performed using the DMol<sup>3</sup> module [28,29]. To describe electron exchange correlation, we employed the Perdew–Burke–Ernzerhof (PBE) functional based on the generalized gradient approximation (GGA) [30], which has been widely used in research on WC MXenes [31,32]. However, it should be noted that GGA function fails to accurately describe the long-range van der Waals (vdW) interaction. Therefore, the Grimme’s dispersion correction (DFT-D3) method was incorporated into our study to account for vdW interactions [4]. The Grimme’s correction method consistently describes all chemically relevant elements within a periodic system and exhibits equal efficacy for both molecules and solids. Furthermore, it achieves a CCSD (T) accuracy, with an error of within 10% [33]. Therefore, the Grimme’s method provides a reliable description of the surface chemistry of MXene systems including the WC family [27,34].

The classical Monkhorst–Pack scheme is employed to generate K-points [35]. In the convergence test, a 4 × 4 × 1 Monkhorst–Pack grid was utilized for K-point sampling [36], and the self-consistent convergence criterion (SCF tolerance) was set to 1 × 10<sup>−5</sup> Ha. To eliminate interlayer interactions, a vacuum layer with a thickness of 20 Å was introduced along the z direction of the WC MXene cell. During geometric optimization, equilibrium geometry was achieved when energy, force, and displacement fall below the thresholds of 2 × 10<sup>−5</sup> Ha, 4 × 10<sup>−3</sup> Ha Å<sup>−1</sup>, and 5 × 10<sup>−3</sup> Å, respectively [37]. The smearing value of 0.005 Ha expedites the convergence rate of electronic structure optimization.

The formation energy ( $E_f$ ) of W<sub>n+1</sub>C<sub>n</sub> MXenes was defined as:

$$E_f = [E_{W_{n+1}C_n} - (n + 1)E_W - nE_C] / (2n + 1)$$

where  $E_{W_{n+1}C_n}$  is the total energy of W<sub>n+1</sub>C<sub>n</sub>,  $E_W$  is the chemical potential of one W atom in the bulk W, and  $E_C$  is the chemical potential of one C atom in graphene.

The adsorption energy ( $E_{ads}$ ) was defined as:

$$E_{ads} = E_{total} - E_{substrate} - E_{adsorbate}$$

where  $E_{\text{total}}$  represents the total energy of the adsorption system,  $E_{\text{substrate}}$  is the total energy of the substrate, and  $E_{\text{adsorbate}}$  is the total energy of the adsorbate.

During the charge and discharge processes, the free energy change ( $\Delta G$ ) of the intermediates at each step can be described as follows:

$$\Delta G = E - E_0 - \Delta n_{\text{Li}}(\mu_{\text{Li}} - eU) + \Delta n_{\text{O}_2}\mu_{\text{O}_2}$$

where  $E$  represents the total energy of the adsorption system at a specific reaction step,  $E_0$  is the total energy of the adsorption system at the initial reaction step, and the  $\Delta n_{\text{Li}}$  and  $\Delta n_{\text{O}_2}$  are the numbers of  $\text{Li}^+$  and  $\text{O}_2$ , respectively. The chemical potential ( $\mu_{\text{Li}}$ ) is defined as the energy of a Li atom in the bulk phase, and the chemical potential ( $\mu_{\text{O}_2}$ ) is defined as the energy of an isolated  $\text{O}_2$  molecule in the gas phase. It has been observed that there is a computational error when calculating the binding energy of  $\text{O}_2$  molecules by using the DFT algorithm [38]. In this study, we determine the total energy of an  $\text{O}_2$  molecule in gas phase by combining experimental  $\text{O}_2$ -binding energy (5.12 eV [39]) with DFT-calculated O atom energy. This is a widely adopted approach in the previous literature [40]. Moreover, any over-binding errors for oxygen molecules are expected to be compensated for free energy profiles of ORR and OER. Therefore, we can accurately determine the qualitative characteristics of free energy profiles of ORR and OER. The term  $-eU$  was included to describe changes in electron potential at potential  $U$ . Additionally, since formation and decomposition of  $\text{Li}_x\text{O}_2$  occur under low temperatures (T) and pressures (P), effects such as entropy (-TS) and volume (PV) are disregarded, which is frequently used in studies in Li- $\text{O}_2$  batteries [41,42]. In this work, we focused on examining the thermodynamic process of the elementary steps of ORR and OER. We assumed that any barriers between these steps are sufficiently small to not impose additional dynamic constraints on starting current at a measurable level. This approach has been widely employed in investigating Li- $\text{O}_2$  batteries [43,44].

The ORR ( $\eta_{\text{ORR}}$ ), OER ( $\eta_{\text{OER}}$ ), and total ( $\eta_{\text{TOT}}$ ) potentials are defined as  $\eta_{\text{ORR}} = U_0 - U_{\text{DC}}$ ,  $\eta_{\text{OER}} = U_{\text{C}} - U_0$ , and  $\eta_{\text{TOT}} = \eta_{\text{ORR}} + \eta_{\text{OER}}$ , respectively. In this definition,  $U_{\text{DC}}$  represents the highest discharge potential that drives the energy downhill for all ORR steps,  $U_{\text{C}}$  represents the lowest charge potential that drives the energy downhill for all OER steps, and  $U_0$  denotes the equilibrium potential ( $\Delta G \leq 0$ ) that facilitates the spontaneous occurrence of ORR/OER [45,46].

The d-band center ( $\varepsilon_{\text{d}}$ ) and p-band center ( $\varepsilon_{\text{p}}$ ) are calculated using formulas:

$$\varepsilon_{\text{d}} = \frac{\int_{-\infty}^{\infty} E\rho_{\text{d}}(E)dE}{\int_{-\infty}^{\infty} \rho_{\text{d}}(E)dE}$$

and

$$\varepsilon_{\text{p}} = \frac{\int_{-\infty}^{\infty} E\rho_{\text{p}}(E)dE}{\int_{-\infty}^{\infty} \rho_{\text{p}}(E)dE}$$

where  $\rho_{\text{d}}(E)$  and  $\rho_{\text{p}}(E)$  denote the densities of d-states and p-states at the energy level  $E$ , respectively.

### 3. Results and Discussion

#### 3.1. Structural Properties of WC MXenes

The crystal structures of optimized  $\text{W}_2\text{C}$ ,  $\text{W}_3\text{C}_2$  and  $\text{W}_4\text{C}_3$  are depicted in Figure 1.  $\text{W}_2\text{C}$  MXene exhibits a hexagonal structure similar to hexagonal  $\text{MoS}_2$  with two surface W layers and an intermediate C layer (Figure 1a). By altering the stacking sequence of the W and C layers according to ABA stacking, the W-C-W sandwich structure of  $\text{W}_2\text{C}$  MXene serves as a foundation for constructing thicker MXenes such as  $\text{W}_3\text{C}_2$  and  $\text{W}_4\text{C}_3$  (Figure 1). Consequently,  $\text{W}_3\text{C}_2$  MXene consists of three W layers and two C layers, while  $\text{W}_4\text{C}_3$  MXene contains four W layers and three C layers. The lattice constants of  $\text{W}_2\text{C}$  MXenes are calculated to be  $a = b = 2.83 \text{ \AA}$ , and the W-C bond length is found to be  $2.126 \text{ \AA}$ ,

which is in excellent agreement with the previously reported results (Lattice constant  $a = b = 2.84 \text{ \AA}$ , and W-C bond length  $2.130 \text{ \AA}$ ) [27,34]. In addition, the formation energy of  $W_2C$ ,  $W_3C_2$ , and  $W_4C_3$  MXenes is calculated to be  $-3.48$ ,  $-3.35$ , and  $-3.33 \text{ eV}$  (see Table S1), respectively, indicating their strong thermodynamic stability [25]. All of these indicate the reliability of the WC-MXene models and calculation methods.

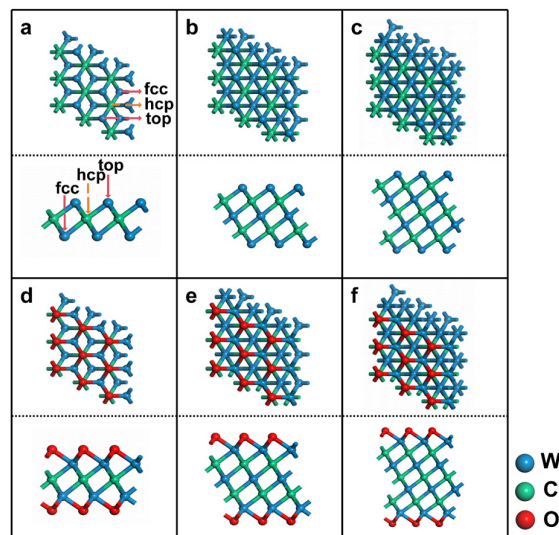


**Figure 1.** Top and side views of (a)  $W_2C$ , (b)  $W_3C_2$ , (c)  $W_4C_3$ , (d)  $W_2CO_2$ , (e)  $W_3C_2O_2$ , and (f)  $W_4C_3O_2$ . Top, hcp, and fcc indicate possible adsorption sites.

The surface modification is commonly employed to introduce functional groups, such as  $-O$ ,  $-F$ , and  $-OH$ , onto the MXene surfaces to improve the interaction between MXenes and adsorbents [47]. Previous studies have demonstrated that oxygen from air can replace  $-F$  and  $-OH$  groups, leading to more stable O-terminated MXenes. This suggests that WC MXenes are highly susceptible to being covered by  $-O$  groups [48–50]. Therefore, we selected  $W_2C$ ,  $W_3C_2$ , and  $W_4C_3$  MXenes with full coverage of  $-O$  groups (i.e.,  $W_2CO_2$ ,  $W_3C_2O_2$  and  $W_4C_3O_2$ , see Figure 1d–f) as probes for surface-functionalized WC MXenes.

The projected state density (PDOS) of the pristine  $W_{n+1}C_n$  and O-terminated  $W_{n+1}C_nO_2$  ( $n = 1, 2, 3$ ) MXenes were plotted to investigate the electronic properties of WC MXenes, as depicted in Figure 2. It can be observed that the total density of states (TDOSs) of both  $W_{n+1}C_n$  and  $W_{n+1}C_nO_2$  intersect with the Fermi level, indicating the high electrical conductivity of  $W_{n+1}C_n$  and  $W_{n+1}C_nO_2$ . With the increasing number of atomic layers of WC MXenes, the intensity of TDOS at the Fermi level increase gradually, suggesting the progressively enhanced conductivity of  $W_{n+1}C_n$  and  $W_{n+1}C_nO_2$  MXenes. Furthermore, the d-band centers of the surface W atoms for  $W_2C$ ,  $W_3C_2$ , and  $W_4C_3$  are calculated to be  $-3.11$ ,  $-3.73$ , and  $-3.90 \text{ eV}$  with respect to the Fermi level, respectively, while the p-band centers of the surface O atoms for  $W_2CO_2$ ,  $W_3C_2O_2$ , and  $W_4C_3O_2$  are calculated to be  $-4.37$ ,  $-4.57$ , and  $-4.61 \text{ eV}$ , respectively. As the atomic layer increases, both the W d band center of  $W_{n+1}C_n$  and the O p band center of  $W_{n+1}C_nO_2$  move downwards and away from the Fermi level, suggesting that the binding strength of the MXene surfaces to the  $Li_xO_2$  intermediate in the  $Li_xO_2$  batteries gradually weakens [51,52]. Therefore, increasing atomic layers of  $W_{n+1}C_n/W_{n+1}C_nO_2$  MXenes is not only beneficial for improving conductivity, but also weakens the adsorption of  $Li_xO_2$  intermediates, thereby preventing their accumulation on the electrode surfaces.

According to Hirshfeld's charge population analyses (Figure 3), the surface W atom of  $W_{n+1}C_n$  MXenes carries a positive charge of  $0.12$ – $0.19 \text{ e}$ , while the sublayer C atom has a negative charge of  $-0.24 \text{ e}$  to  $-0.25 \text{ e}$ , suggesting electron transfer from W to C. Therefore, the surface W atom in  $W_{n+1}C_n$  is a positive charge center, showing electrophilicity. When the  $-O$  groups are introduced on the surface of  $W_{n+1}C_n$ , the positive charge on the W atom

of  $W_{n+1}C_nO_2$  increases to  $0.30 e \sim 0.34 e$ , and the  $-O$  group has a negative charge of  $-0.20 e$ , which indicates that strong electron transfer from  $W$  to  $O$  occurs in  $W_{n+1}C_nO_2$ . Thus, the surface  $O$  atom in  $W_{n+1}C_nO_2$  forms a negative charge center, which is nucleophilic. This situation can be further confirmed with the differential electron density maps. As shown in Figure 4, an electron depletion region (yellow) is observed on the surface  $W$  atoms of  $W_{n+1}C_n$ , while an electron accumulation region (blue) is located on the surface  $O$  atoms of  $W_{n+1}C_nO_2$ , due to the different electronegativity between non-metallic oxygen and metallic  $W$ . Consequently, oxygen functionalization transforms  $WC$  MXenes from an electrophilic surface of  $W_{n+1}C_n$  to a nucleophilic surface of  $W_{n+1}C_nO_2$ , thereby regulating the adsorption and activation of intermediates on the MXene surfaces.

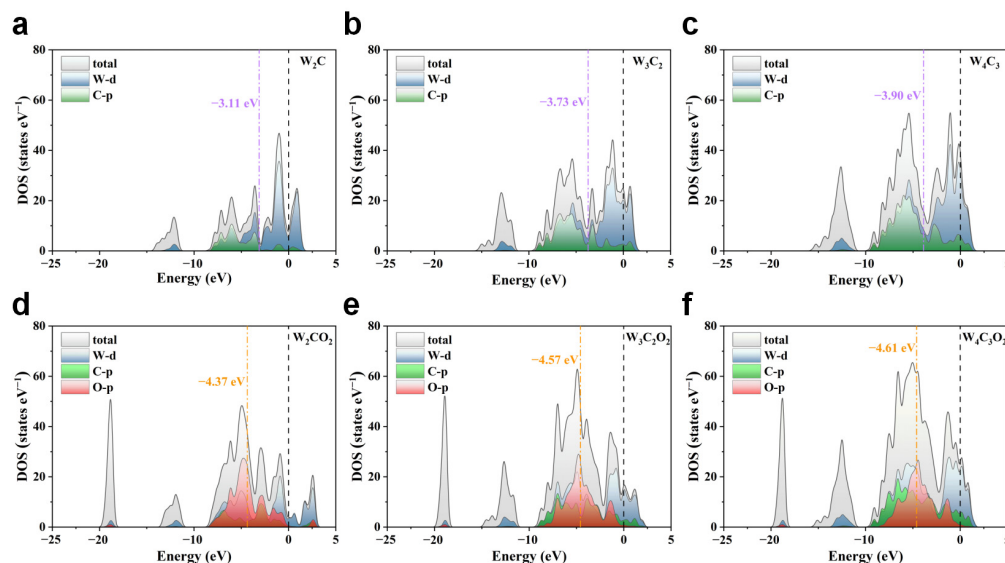


**Figure 2.** Projected density of states (PDOS) of (a–c)  $W_{n+1}C_n$  and (d–f)  $W_{n+1}C_nO_2$ . The Fermi level marked by the black dashed line is set as energy zero.

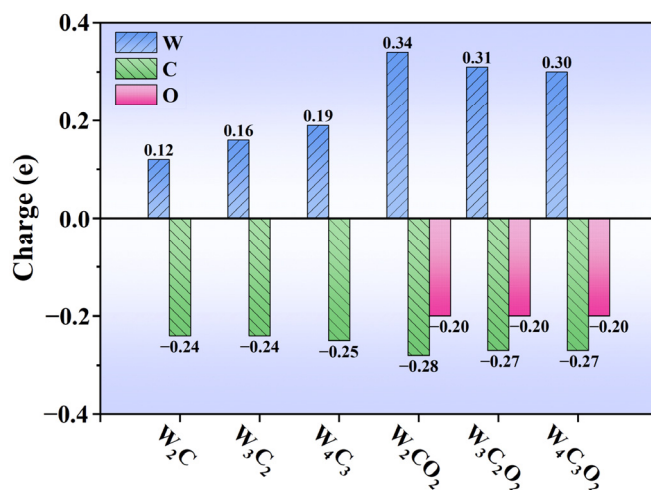


**Figure 3.** The Hirshfeld charge (in  $e$ ) of surface  $W$  atoms, sublayer  $C$  atoms, and surface  $O$  groups of  $W_{n+1}C_n$  and  $W_{n+1}C_nO_2$ .

The adsorption of the  $Li_xO_2$  ( $x = 1, 2,$  and  $4$ ) intermediates was examined on  $W_{n+1}C_n$  and  $W_{n+1}C_nO_2$ . As shown in Figure S1, the  $Li_xO_2$  intermediates exhibit similar adsorption configurations on the  $W_{n+1}C_n$  surfaces, where the surface  $W$  atom binds to the  $O$  atom in  $Li_xO_2$ . This is because the electrophilic  $W$  atoms on the  $W_{n+1}C_n$  surface prefer to bind with the negatively charged  $O$  atoms in  $Li_xO_2$ . The strong interaction between the oxygen atom and the surface  $W$  atom promotes the activation of the  $O-O$  bond in the adsorbed

$\text{Li}_x\text{O}_2^*$ . Consequently, the O-O bonds in the adsorbed  $\text{Li}_x\text{O}_2^*$  on  $\text{W}_{n+1}\text{C}_n$  are apparently longer than the Li-O bonds (see Table S3), which hinders the deintercalation of lithium during the charge–discharge processes. Alternatively, the surface O atoms of  $\text{W}_{n+1}\text{C}_n\text{O}_2$  directly adsorb the Li atoms of  $\text{Li}_x\text{O}_2$  (see Figure S2), because the nucleophilic surface O atoms tend to bind with positively charged Li atoms. This results in a shortened O-O bond and an elongated Li-O bond after  $\text{Li}_x\text{O}_2$  adsorbs on the surface of  $\text{W}_{n+1}\text{C}_n\text{O}_2$  (Table S4), thereby facilitating the deintercalation of lithium during the charge–discharge processes. Thus, oxygen functionalization can effectively improve the lithium deintercalation process on the WC MXene surfaces.

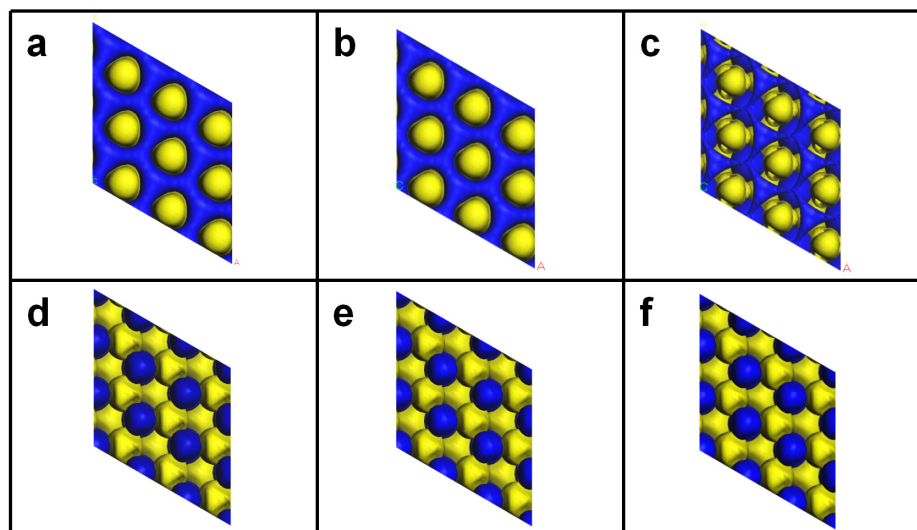


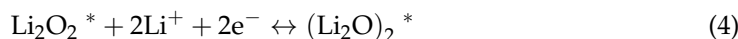
**Figure 4.** Differential electron density maps of (a)  $\text{W}_2\text{C}$ , (b)  $\text{W}_3\text{C}_2$ , (c)  $\text{W}_4\text{C}_3$ , (d)  $\text{W}_2\text{CO}_2$ , (e)  $\text{W}_3\text{C}_2\text{O}_2$ , and (f)  $\text{W}_4\text{C}_3\text{O}_2$ .

The adsorption energies of the  $\text{Li}_x\text{O}_2$  ( $x = 1, 2$ , and 4) intermediates on  $\text{W}_{n+1}\text{C}_n$  and  $\text{W}_{n+1}\text{C}_n\text{O}_2$  are listed in Table S2. Compared with the W surface of  $\text{W}_{n+1}\text{C}_n$ , the O surface of  $\text{W}_{n+1}\text{C}_n\text{O}_2$  exhibits weaker adsorption towards the  $\text{Li}_x\text{O}_2$  intermediates. This is in good accordance with previous theoretical reports, where the oxide layer behaves as a passivation layer on the  $\text{TiC}(111)$ ,  $\text{ZrC}(111)$ ,  $\alpha\text{-MoC}(001)$ , and  $\text{Mo}_2\text{C}(001)$  systems upon  $\text{Li}_2\text{O}_2$  adsorption [52]. Furthermore, with an increasing number of atomic layers, the adsorption energy of the  $\text{Li}_x\text{O}_2$  intermediates on both  $\text{W}_{n+1}\text{C}_n$  and  $\text{W}_{n+1}\text{C}_n\text{O}_2$  MXenes is gradually weakened. The situation can be attributed to the downward shift of the d-band centers of surface W atoms in  $\text{W}_{n+1}\text{C}_n$  and the p-band centers of surface O atoms in  $\text{W}_{n+1}\text{C}_n\text{O}_2$  with the increasing atomic layers. As shown in Figure 2, the d-band center of surface W atoms is shifted from  $-3.11$  eV in  $\text{W}_2\text{C}$  to  $-3.90$  eV in  $\text{W}_4\text{C}_3$ , while the p-band center of surface O atoms is shifted from  $-4.37$  eV in  $\text{W}_2\text{CO}_2$  to  $-4.61$  eV in  $\text{W}_4\text{C}_3\text{O}_2$ . The downward shift of the band center increases the electron filling on the anti-bonding states between MXenes and the adsorbate, resulting in a weakened binding interaction. Hence, both oxygen functionalization and increasing atomic layers can weaken the interaction between WC MXenes and the  $\text{Li}_x\text{O}_2$  intermediates, avoiding their accumulation caused by their excessive adsorption.

### 3.2. Evaluation of Catalytic Activity

Based on the reported experimental and theoretical results [2,3,47], we investigated three surface reaction steps (Equations (2)–(4)) to simulate the ORR/OER process on WC MXenes. During the discharge process, the  $\text{O}_2^*$  species on the surface of WC MXene cathodes undergoes initial metallization with ( $\text{Li}^+ + \text{e}^-$ ) to form adsorbed  $\text{LiO}_2^*$ . Subsequently,  $\text{LiO}_2^*$  undergoes a second metallization with ( $\text{Li}^+ + \text{e}^-$ ) to generate  $\text{Li}_2\text{O}_2^*$ . Finally,  $\text{Li}_2\text{O}_2^*$  further reacts with ( $\text{Li}^+ + \text{e}^-$ ) to yield the final product  $(\text{Li}_2\text{O})_2^*$ . The OER at the cathode of a Li- $\text{O}_2$  battery during charging is essentially the reverse process of the aforementioned

ORR. In the OER process, the ultimate adsorption product  $(\text{Li}_2\text{O})_2^*$  gradually decomposes into  $\text{O}_2^*$ , which then dissociates from the surface of WC MXenes.



Subsequently, we constructed the free energy diagram to illustrate the ORR/OER process on  $\text{W}_{n+1}\text{C}_n$  and  $\text{W}_{n+1}\text{C}_n\text{O}_2$  (Figure 5). The purple arrows in the graph represent the discharge-oriented ORR process from left to right, and the orange arrows indicate the charging-driven OER process from right to left. The nucleation of  $(\text{Li}_2\text{O})_2$  on WN MXenes follows three steps:  $\text{O}_2^* \rightarrow \text{LiO}_2^* \rightarrow \text{Li}_2\text{O}_2^* \rightarrow (\text{Li}_2\text{O})_2^*$ . Notably, at open circuit voltage ( $U = 0 \text{ V}$ ), both  $\text{W}_{n+1}\text{C}_n$  and  $\text{W}_{n+1}\text{C}_n\text{O}_2$  (the black path in Figure 5) exhibit a downhill trend in their free energy profiles for all three metallization steps of ORR, suggesting the spontaneous nucleation of  $(\text{Li}_2\text{O})_2$  on the surface of WC MXenes. Conversely, during the reverse OER process, the decomposition of  $(\text{Li}_2\text{O})_2$  is endothermic on both  $\text{W}_{n+1}\text{C}_n$  and  $\text{W}_{n+1}\text{C}_n\text{O}_2$  MXenes. Furthermore, the whole free energy change ( $\Delta G(\text{O}_2^* \rightarrow (\text{Li}_2\text{O})_2^*)$ ) of the  $\text{O}_2^* \rightarrow (\text{Li}_2\text{O})_2^*$  process decreases with the increasing atomic layers of  $\text{W}_{n+1}\text{C}_n$  and  $\text{W}_{n+1}\text{C}_n\text{O}_2$ . This is because the WC MXenes exhibit a weakened affinity towards  $\text{Li}_x\text{O}_2$  intermediates as the number of atomic layers increases. These findings suggest that as the number of atomic layers increases, it becomes easier for  $(\text{Li}_2\text{O})_2$  products to undergo decomposition on the WC MXene surfaces. Moreover, compared to the pristine  $\text{W}_{n+1}\text{C}_n$ ,  $\Delta G(\text{O}_2 \rightarrow (\text{Li}_2\text{O})_2^*)$  for the oxygen-functionalized  $\text{W}_{n+1}\text{C}_n\text{O}_2$  is significantly reduced, which is further beneficial for the  $(\text{Li}_2\text{O})_2$  decomposition. Therefore, both increasing atomic layers and oxygen functionalization can promote the de-lithiation of  $(\text{Li}_2\text{O})_2$  products, thereby accelerating the electrochemical process during charging.

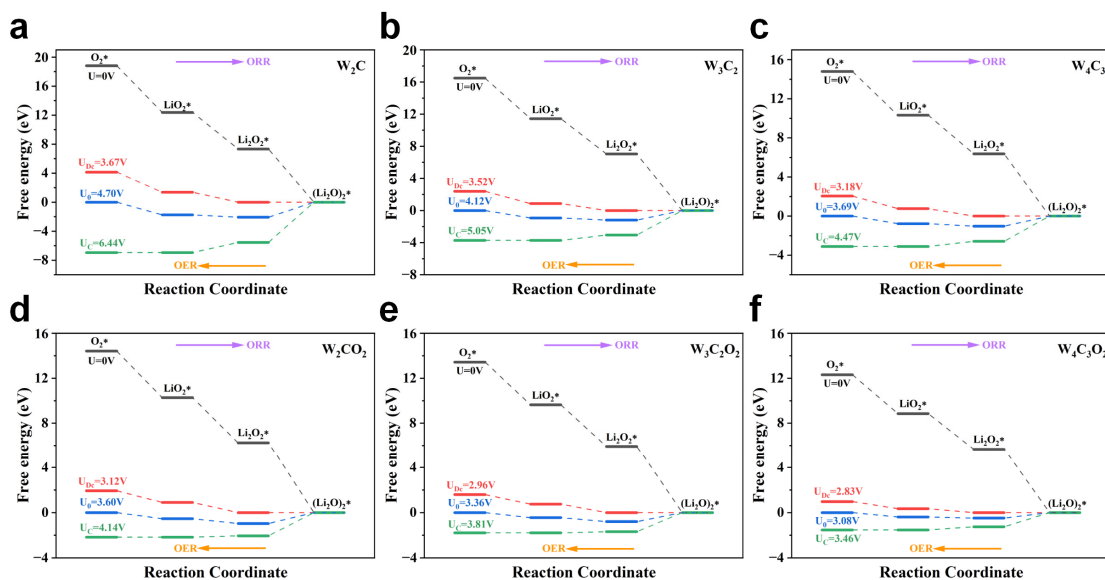


**Figure 5.** Free energy diagram of the ORR/OER process for  $\text{Li}_x\text{O}_2$  intermediates on (a)  $\text{W}_2\text{C}$ , (b)  $\text{W}_3\text{C}_2$ , (c)  $\text{W}_4\text{C}_3$ , (d)  $\text{W}_2\text{CO}_2$ , (e)  $\text{W}_3\text{C}_2\text{O}_2$ , and (f)  $\text{W}_4\text{C}_3\text{O}_2$ . \* indicates that the intermediate is in an adsorbed state.

In Figure 5,  $U_{\text{DC}}$  represents the maximum discharge potential driving the energy of all ORR steps to exhibit a downward trend along the red path from left to right, while  $U_{\text{C}}$  represents the minimum charging potential driving the energy of all OER steps to decrease along the green path from right to left. The equilibrium potential  $U_0$  applied in the blue path facilitates achieving equilibrium in the electrochemical ORR/OER process. With an increase

in atomic layer number, the  $\Delta G(\text{O}_2^* \rightarrow (\text{Li}_2\text{O})_2^*)$  of  $\text{W}_{n+1}\text{C}_n$  MXenes gradually decreases, and therefore the required  $U_0$  decreases as well. The values of  $U_0$  are calculated to be 4.70, 4.12, and 3.70 V for  $\text{W}_2\text{C}$ ,  $\text{W}_3\text{C}_2$ , and  $\text{W}_4\text{C}_3$ , respectively (Figure 5a–c). After surface oxygen functionalization, the  $\Delta G(\text{O}_2^* \rightarrow (\text{Li}_2\text{O})_2^*)$  of  $\text{W}_{n+1}\text{C}_n\text{O}_2$  further decreases significantly, and thus the corresponding  $U_0$  for  $\text{W}_2\text{CO}_2$ ,  $\text{W}_3\text{C}_2\text{O}_2$ , and  $\text{W}_4\text{C}_3\text{O}_2$  is decreased to be 3.60, 3.36, and 3.08 V, respectively (Figure 5d–f). Consequently, the  $\text{W}_4\text{C}_3\text{O}_2$  MXene has a minimum  $U_0$  among  $\text{W}_{n+1}\text{C}_n$  and  $\text{W}_{n+1}\text{C}_n\text{O}_2$  MXenes.

When  $U_0$  is applied to the electrochemical processes on  $\text{W}_{n+1}\text{C}_n$  and  $\text{W}_{n+1}\text{C}_n\text{O}_2$ , the formation steps of  $\text{Li}_2\text{O}_2^*$  and  $\text{LiO}_2^*$  along the ORR pathway are still downhill in the free energy profiles (the blue path in Figure 5). However, the last  $(\text{Li}_2\text{O})_2^*$  formation step shows an upward trend, suggesting it forms the rate-determining step (RDS) of the ORR pathway on both  $\text{W}_{n+1}\text{C}_n$  and  $\text{W}_{n+1}\text{C}_n\text{O}_2$ . Compared to the downhill step of the  $(\text{Li}_2\text{O})_2^*$  decomposition, the decomposition of  $\text{Li}_2\text{O}_2^*$  and  $\text{LiO}_2^*$  is uphill along the OER pathway in the free energy profiles. Furthermore, the decomposition of  $\text{LiO}_2^*$  requires a higher energy input than that of  $\text{Li}_2\text{O}_2^*$ , suggesting that it serves as the RDS of OER on  $\text{W}_{n+1}\text{C}_n$  and  $\text{W}_{n+1}\text{C}_n\text{O}_2$ .

The overpotential  $\eta$  is defined as the minimum  $|U - U_0|$  that makes all the electrochemical steps downhill in free energy and serves as a crucial indicator for assessing the catalytic performance of a catalyst [51]. The smaller the value of  $\eta$ , the lower the actual voltage required to achieve a target current density, resulting in reduced energy consumption and enhanced catalytic activity [45,53]. In this study, we calculated the ORR ( $\eta_{\text{ORR}}$ ), OER ( $\eta_{\text{OER}}$ ), and total ( $\eta_{\text{TOT}}$ ) overpotentials by  $\eta_{\text{ORR}} = U_0 - U_{\text{DC}}$ ,  $\eta_{\text{OER}} = U_{\text{C}} - U_0$ , and  $\eta_{\text{TOT}} = \eta_{\text{ORR}} + \eta_{\text{OER}}$ , respectively. Detailed data on overpotentials are presented in Figure 6. The overpotentials ( $\eta_{\text{OER}}/\eta_{\text{ORR}}/\eta_{\text{TOT}}$ ) of the pristine  $\text{W}_{n+1}\text{C}_n$  follow the order:  $\text{W}_4\text{C}_3$  (0.78 V/0.51 V/1.29 V) <  $\text{W}_3\text{C}_2$  (0.93 V/0.60 V/1.53 V) <  $\text{W}_2\text{C}$  (1.74 V/1.03 V/2.77 V), suggesting that the  $\text{W}_{n+1}\text{C}_n$  MXenes show a decrease trend in overpotentials with an increasing number of atomic layers. After the WC surfaces are covered with O groups, there is a significant decrease in overpotentials. The values of  $\eta_{\text{OER}}$ ,  $\eta_{\text{ORR}}$ , and  $\eta_{\text{TOT}}$  are decreased in the order of  $\text{W}_4\text{C}_3\text{O}_2$  (0.38 V/0.25 V/0.63 V) <  $\text{W}_3\text{C}_2\text{O}_2$  (0.45 V/0.39 V/0.84 V) <  $\text{W}_2\text{CO}_2$  (0.54 V/0.48 V/1.02 V). Moreover, the values of  $\eta_{\text{OER}}$  for  $\text{W}_{n+1}\text{C}_n$  and  $\text{W}_{n+1}\text{C}_n\text{O}_2$  MXenes are higher than those of  $\eta_{\text{ORR}}$ , indicating the slower kinetics of the OER during the charging process, which may lead to poor cyclic stability [54]. This is attributed to the strong adsorption of the  $\text{Li}_x\text{O}_2$  produced during the discharge process, which makes it difficult to reversibly decompose, resulting in continuous accumulation [55,56]. Among all considered WC MXenes,  $\text{W}_4\text{C}_3\text{O}_2$  exhibits the lowest OER, ORR, and total overpotentials (0.38, 0.25, and 0.63 V). Furthermore, it is worth noting that the overpotentials ( $\eta_{\text{OER}}$ ,  $\eta_{\text{ORR}}$ , and  $\eta_{\text{TOT}}$ ) of  $\text{W}_4\text{C}_3\text{O}_2$  are lower than those of  $\text{Nb}_2\text{CO}_2$  MXene (0.81, 0.50, and 1.31 V) [57],  $\text{Se@NiO/CC}$  (0.32, 0.36, and 0.68 V) [58],  $\text{SAsSe-Ti}_3\text{C}_2$  (0.59, 0.29, and 0.88 V) [59],  $\text{CuCo}_2\text{S}_4$  (0.35, 0.30, and 0.65 V) [60],  $\text{NiSA-Co}_3\text{O}_4$  (1.09, 0.21, and 1.30 V) [12],  $\text{CoS}_2$  (0.89, 0.47, and 1.36 V) [61], and other recently reported two-dimensional materials [45,62,63]. These suggest that the  $\text{W}_4\text{C}_3\text{O}_2$  MXene shows excellent catalytic performance as a cathode catalyst for Li-O<sub>2</sub> batteries.

To further investigate the relationship between the adsorption property of  $\text{Li}_x\text{O}_2$  and the overpotentials, we plotted the correlation between the adsorption energy ( $E_{\text{ads}}$ ) of RDS intermediates and  $\eta_{\text{ORR}}/\eta_{\text{OER}}$  in the ORR/OER process for WC MXenes (Figure 7). In the ORR process, the reduction of  $\text{Li}_2\text{O}_2^*$  to  $(\text{Li}_2\text{O})_2^*$  serves as the RDS on both  $\text{W}_{n+1}\text{C}_n$  and  $\text{W}_{n+1}\text{C}_n\text{O}_2$  MXenes, and thus the adsorption energy of  $\text{Li}_2\text{O}_2^*$  ( $E_{\text{ads}}(\text{Li}_2\text{O}_2^*)$ ) plays a key role in  $\eta_{\text{ORR}}$ . As depicted in Figure 7a, there is a linear correlation between  $E_{\text{ads}}(\text{Li}_2\text{O}_2^*)$  and  $\eta_{\text{ORR}}$  for WC MXenes. The values of  $\eta_{\text{ORR}}$  decrease with the decrease of the adsorption energy of  $\text{Li}_2\text{O}_2^*$  on  $\text{W}_{n+1}\text{C}_n$  and  $\text{W}_{n+1}\text{C}_n\text{O}_2$  MXenes. Reducing the adsorption strength of  $\text{Li}_2\text{O}_2^*$  is beneficial for further metallization to produce  $(\text{Li}_2\text{O})_2^*$ , resulting in a reduced value of the corresponding  $\eta_{\text{ORR}}$  for WC MXenes. In the OER process, the decomposition of  $\text{LiO}_2^*$  into  $\text{O}_2^*$  acts as the RDS on WC MXenes. Thus, the adsorption energy of  $\text{LiO}_2^*$  ( $E_{\text{ads}}(\text{LiO}_2^*)$ ) is important in determining  $\eta_{\text{OER}}$ . As shown in Figure 7b,  $E_{\text{ads}}(\text{LiO}_2^*)$

and  $\eta_{\text{OER}}$  exhibit a linear relationship for  $W_{n+1}C_n$  and  $W_{n+1}C_nO_2$  MXenes. A weaker  $E_{\text{ads}}(\text{LiO}_2^*)$  can promote the decomposition of  $\text{LiO}_2^*$ , leading to a lower value of the corresponding  $\eta_{\text{OER}}$ . These findings demonstrate that the reduced adsorption energy of the RDS intermediates ( $\text{LiO}_2^*$  and  $\text{Li}_2\text{O}_2^*$ ) has a positive effect on reducing overpotentials. By lowering the energy band center, oxygen functionalization and increasing the atomic layer can effectively reduce the adsorption strength of the RDS intermediates ( $\text{Li}_2\text{O}_2^*$  and  $\text{LiO}_2^*$ ), thereby reducing the ORR and OER overpotentials.

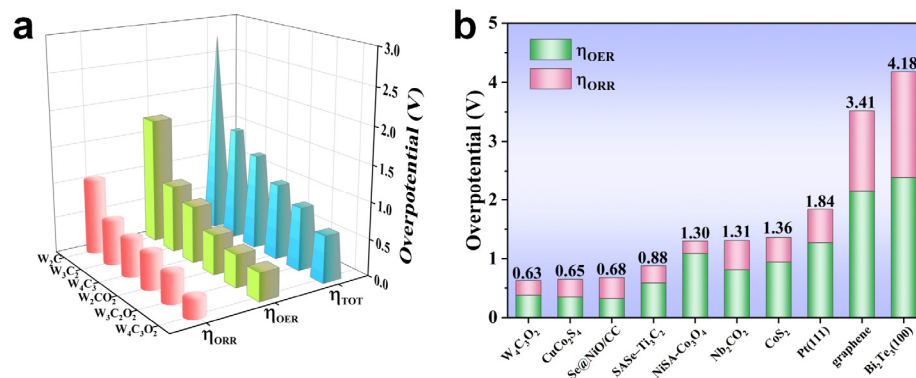


**Figure 6.** (a) The ORR ( $\eta_{\text{ORR}}$ ), OER ( $\eta_{\text{OER}}$ ), and total ( $\eta_{\text{TOT}}$ ) overpotentials for WC MXenes. (b) Comparison of overpotentials for  $W_4C_3O_2$  MXene with other materials.

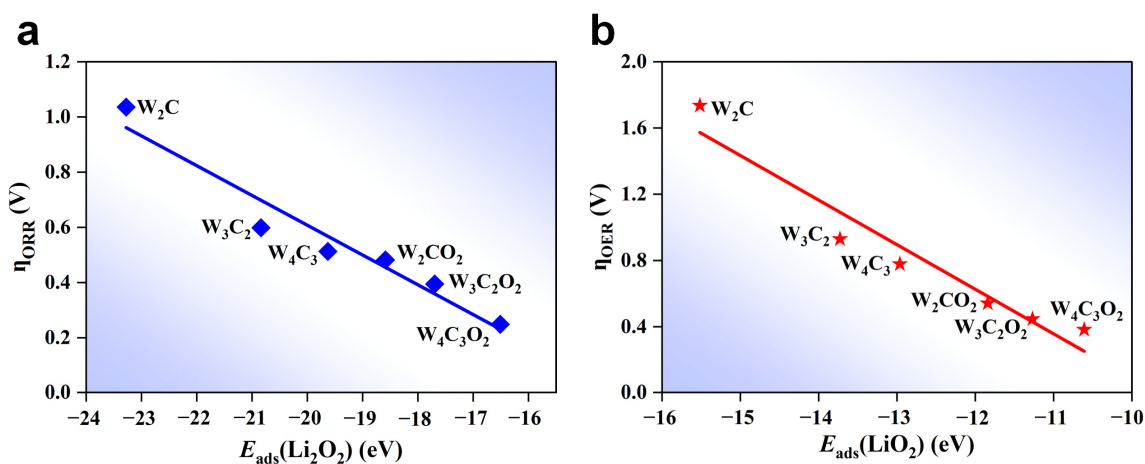


**Figure 7.** (a) The ORR overpotential ( $\eta_{\text{ORR}}$ ) as the function of the adsorption energy of  $\text{Li}_2\text{O}_2$  ( $E_{\text{ads}}(\text{Li}_2\text{O}_2)$ ). (b) The OER overpotential ( $\eta_{\text{OER}}$ ) as the function of the adsorption energy of  $\text{LiO}_2$  ( $E_{\text{ads}}(\text{LiO}_2)$ ).

#### 4. Conclusions

In this work, the models of pristine  $W_{n+1}C_n$  and oxygen-functionalized  $W_{n+1}C_nO_2$  MXenes were constructed, and their catalytic performance as cathodes for Li- $\text{O}_2$  batteries was evaluated using first principles calculations. The TDOS analyses at the Fermi level confirm the excellent electrical conductivity of both  $W_{n+1}C_n$  and  $W_{n+1}C_nO_2$ , which is further enhanced with increasing atomic layers. The oxygen functionalization alters the electronic properties of WC MXenes from the electrophilic W surface of  $W_{n+1}C_n$  to the nucleophilic O surface of  $W_{n+1}C_nO_2$ , which facilitates the Li-O bond activation and thus promotes Li deintercalation during the charge–discharge process. Compared to the pristine  $W_{n+1}C_n$ , the oxygen-functionalized  $W_{n+1}C_nO_2$  has a significantly reduced adsorption energy towards  $\text{Li}_x\text{O}_2$ , resulting in lower overpotentials of  $\eta_{\text{OER}}$ ,  $\eta_{\text{ORR}}$ , and  $\eta_{\text{TOT}}$ . As the number of atomic layers in WC MXenes increases, the adsorption energy of  $\text{Li}_x\text{O}_2$  is further decreased, leading to a reduction in  $\eta_{\text{OER}}$ ,  $\eta_{\text{ORR}}$ , and  $\eta_{\text{TOT}}$ . The O-terminated  $W_4C_3O_2$  MXene shows superior electrical conductivity and remarkably low overpotentials (0.38 V

for  $\eta_{\text{OER}}$ , 0.25 V for  $\eta_{\text{ORR}}$ , and 0.63 V for  $\eta_{\text{TOT}}$ ), highlighting its huge potential as a cathode catalyst for Li-O<sub>2</sub> batteries. The study indicates that the WC MXenes can serve as cathode materials for Li-O<sub>2</sub> batteries, and W<sub>4</sub>C<sub>3</sub>O<sub>2</sub> is identified as a high-performance cathode catalyst material. This finding is of great importance for the design and manufacture of cathode catalysts used in Li-O<sub>2</sub> batteries.

**Supplementary Materials:** The following supporting information can be downloaded at: <https://www.mdpi.com/article/10.3390/nano14080666/s1>, Figure S1: the top and side views of the adsorption configuration of LiO<sub>2</sub> on WC MXenes; Figure S2: the top and side views of the adsorption configuration of Li<sub>2</sub>O<sub>2</sub> on WC MXenes; Table S1: formation energy of W<sub>2</sub>C, W<sub>3</sub>C<sub>2</sub>, and W<sub>4</sub>C<sub>3</sub>; Table S2: the adsorption energy of Li<sub>x</sub>O<sub>2</sub> on W<sub>n+1</sub>C<sub>n</sub> and W<sub>n+1</sub>C<sub>n</sub>O<sub>2</sub>; Table S3: the average length of the Li-O and O-O bonds in LiO<sub>2</sub>/Li<sub>2</sub>O<sub>2</sub> and the adsorbed distance of LiO<sub>2</sub>/Li<sub>2</sub>O<sub>2</sub> to W<sub>n+1</sub>C<sub>n</sub>; Table S4: the average length of the Li-O and O-O bonds in LiO<sub>2</sub>/Li<sub>2</sub>O<sub>2</sub> and the adsorbed distance of LiO<sub>2</sub>/Li<sub>2</sub>O<sub>2</sub> to W<sub>n+1</sub>C<sub>n</sub>O<sub>2</sub>; Table S5:  $U_{\text{Dc}}$ ,  $U_0$ ,  $U_c$ ,  $\eta_{\text{ORR}}$ ,  $\eta_{\text{OER}}$ , and  $\eta_{\text{TOT}}$  for W<sub>n+1</sub>C<sub>n</sub> and W<sub>n+1</sub>C<sub>n</sub>O<sub>2</sub>.

**Author Contributions:** L.Z. (Liwei Zhu)—Investigation, Writing; J.W.—Data curation; J.L.—Validation; R.W.—Visualization; M.L.—Formal analysis; T.W.—Investigation; Y.Z.—Validation, Visualization; J.X.—Funding acquisition, Resources, Supervision; L.Z. (Lianming Zhao)—Supervision, Funding acquisition, Project administration, Writing—review and editing. All authors have read and agreed to the published version of the manuscript.

**Funding:** This research was funded by the Shandong Provincial Natural Science Foundation (No. ZR2022MB094).

**Data Availability Statement:** Data will be made available on request.

**Conflicts of Interest:** The authors declare that they have no known competing financial interest or personal relationships that could have appeared to influence the work reported in this paper.

## References

1. Mu, X.; Xia, C.; Gao, B.; Guo, S.; Zhang, X.; He, J.; Wang, Y.; Dong, H.; He, P.; Zhou, H. Two-Dimensional Mo-Based Compounds for the Li-O<sub>2</sub> Batteries: Catalytic Performance and Electronic Structure Studies. *Energy Storage Mater.* **2021**, *41*, 650–655. [CrossRef]
2. Xia, Q.; Li, D.; Zhao, L.; Wang, J.; Long, Y.; Han, X.; Zhou, Z.; Liu, Y.; Zhang, Y.; Li, Y. Recent Advances in Heterostructured Cathodic Electrocatalysts for Non-Aqueous Li-O<sub>2</sub> Batteries. *Chem. Sci.* **2022**, *13*, 2841–2856. [CrossRef] [PubMed]
3. Du, D.; Zhu, Z.; Chan, K.-Y.; Li, F.; Chen, J. Photoelectrochemistry of Oxygen in Rechargeable Li-O<sub>2</sub> Batteries. *Chem. Soc. Rev.* **2022**, *51*, 1846–1860. [CrossRef] [PubMed]
4. Zhang, Y.; Zhang, S.; Li, H.; Lin, Y.; Yuan, M.; Nan, C.; Chen, C. Tunable Oxygen Vacancies of Cobalt Oxides in Lithium-Oxygen Batteries: Morphology Control of Discharge Product. *Nano Lett.* **2023**, *23*, 9119–9125. [CrossRef]
5. Sun, Z.; Lin, X.; Wang, C.; Hu, A.; Hou, Q.; Tan, Y.; Dou, W.; Yuan, R.; Zheng, M.; Dong, Q. High-Performance Lithium-Oxygen Batteries Using a Urea-Based Electrolyte with Kinetically Favorable One-Electron Li<sub>2</sub>O<sub>2</sub> Oxidation Pathways. *Angew. Chem.* **2022**, *134*, E202207570. [CrossRef]
6. Xing, S.; Zhang, Z.; Dou, Y.; Li, M.; Wu, J.; Zhang, Z.; Zhou, Z. An Efficient Multifunctional Soluble Catalyst for Li-O<sub>2</sub> Batteries. *CCS Chem.* **2023**. [CrossRef]
7. Zhao, W.; Wang, J.; Yin, R.; Li, B.; Huang, X.; Zhao, L.; Qian, L. Single-Atom Pt Supported on Holey Ultrathin G-C<sub>3</sub>N<sub>4</sub> Nanosheets as Efficient Catalyst for Li-O<sub>2</sub> Batteries. *J. Colloid Interface Sci.* **2020**, *564*, 28–36. [CrossRef]
8. Zhou, Y.; Gu, Q.; Yin, K.; Li, Y.; Tao, L.; Tan, H.; Yang, Y.; Guo, S. Engineering Eg Orbital Occupancy of Pt with Au Alloying Enables Reversible Li-O<sub>2</sub> Batteries. *Angew. Chem. Int. Ed.* **2022**, *61*, E202201416. [CrossRef] [PubMed]
9. Cui, X.; Luo, Y.; Zhou, Y.; Dong, W.; Chen, W. Application of Functionalized Graphene in Li-O<sub>2</sub> Batteries. *Nanotechnology* **2021**, *32*, 132003. [CrossRef]
10. Dang, C.; Feng, P.; He, S.; Zhao, L.; Shan, A.; Li, M.; Kong, L.; Gao, L. Nicop Based Carbon Nanotube Heterostructure for Improved Oxygen Redox Reaction Kinetics in Li-O<sub>2</sub> Batteries. *Electrochim. Acta* **2023**, *462*, 142771. [CrossRef]
11. Li, Y.; Qin, J.; Ding, Y.; Ma, J.; Das, P.; Liu, H.; Wu, Z.-S.; Bao, X. Two-Dimensional Mn<sub>3</sub>O<sub>4</sub> Nanosheets with Dominant (101) Crystal Planes on Graphene as Efficient Oxygen Catalysts for Ultrahigh Capacity and Long-Life Li-O<sub>2</sub> Batteries. *ACS Catal.* **2022**, *12*, 12765–12773. [CrossRef]
12. Lian, Z.; Lu, Y.; Ma, S.; Li, Z.; Liu, Q. Metal Atom-Doped Co<sub>3</sub>O<sub>4</sub> Nanosheets for Li-O<sub>2</sub> Battery Catalyst: Study on the Difference of Catalytic Activity. *Chem. Eng. J.* **2022**, *445*, 136852. [CrossRef]
13. Zhang, L.; Zhao, C.; Kong, X.; Yu, S.; Zhang, D.; Liu, W. Construction of Co-NC@ Mo<sub>2</sub>C Hetero-Interfaces for Improving the Performance of Li-O<sub>2</sub> Batteries. *Electrochim. Acta* **2023**, *446*, 142096. [CrossRef]

14. Meng, X.; Liao, K.; Dai, J.; Zou, X.; She, S.; Zhou, W.; Ye, F.; Shao, Z. Ultralong Cycle Life Li–O<sub>2</sub> Battery Enabled by a MOF-Derived Ruthenium–Carbon Composite Catalyst with a Durable Regenerative Surface. *ACS Appl. Mater. Interfaces* **2019**, *11*, 20091–20097. [[CrossRef](#)] [[PubMed](#)]
15. Li, N.; Chang, Z.; Zhong, M.; Fu, Z.-X.; Luo, J.; Zhao, Y.-F.; Li, G.-B.; Bu, X.-H. Functionalizing MOF with Redox-Active Tetrazine Moiety for Improving the Performance as Cathode of Li–O<sub>2</sub> Batteries. *CCS Chem.* **2021**, *3*, 1297–1305. [[CrossRef](#)]
16. Zheng, X.; Yuan, M.; Huang, X.; Li, H.; Sun, G. In Situ Decoration of Cop/Ti<sub>3</sub>C<sub>2</sub>T<sub>x</sub> Composite as Efficient Electrocatalyst for Li-Oxygen Battery. *Chin. Chem. Lett.* **2023**, *34*, 107152. [[CrossRef](#)]
17. Teng, K.; Tang, W.; Qi, R.; Li, B.; Deng, Y.; Zhou, M.; Wu, M.; Zhang, J.; Liu, R.; Zhang, L. Nitrogen-Deficient G-C<sub>3</sub>N<sub>4</sub> Compounded with NiCo<sub>2</sub>S<sub>4</sub> (NiCo<sub>2</sub>S<sub>4</sub>@ND-CN) as a Bifunctional Electrocatalyst for Boosting the Activity of Li–O<sub>2</sub> Batteries. *Catal. Today* **2023**, *409*, 23–30. [[CrossRef](#)]
18. Xu, H.; Zheng, R.; Du, D.; Ren, L.; Li, R.; Wen, X.; Zhao, C.; Shu, C. V<sub>2</sub>C Mxene Enriched with-O Termination as High-Efficiency Electrocatalyst for Lithium-Oxygen Battery. *Appl. Mater. Today* **2022**, *27*, 101464. [[CrossRef](#)]
19. Tariq, H.A.; Nisar, U.; Abraham, J.J.; Ahmad, Z.; Alqaradawi, S.; Kahraman, R.; Shakoor, R. TiO<sub>2</sub> Encrusted Mxene as a High-Performance Anode Material for Li-Ion Batteries. *Appl. Surf. Sci.* **2022**, *583*, 152441. [[CrossRef](#)]
20. Zhang, P.; Li, J.; Yang, D.; Soomro, R.A.; Xu, B. Flexible Carbon Dots-Intercalated Mxene Film Electrode with Outstanding Volumetric Performance for Supercapacitors. *Adv. Funct. Mater.* **2023**, *33*, 2209918. [[CrossRef](#)]
21. Tu, W.; Chen, K.; Zhu, L.; Zai, H.E.B.; Ke, X.; Chen, C.; Sui, M.; Chen, Q.; Li, Y. Tungsten-Doping-Induced Surface Reconstruction of Porous Ternary Pt-Based Alloy Electrocatalyst for Oxygen Reduction. *Adv. Funct. Mater.* **2019**, *29*, 1807070. [[CrossRef](#)]
22. Du, Y.; Chen, W.; Zhou, L.; Hu, R.; Wang, S.; Li, X.; Xie, Y.; Yang, L.; Liu, Y.; Liu, Z. One-Step, in Situ Formation of WN–W<sub>2</sub>C Heterojunctions Implanted on N Doped Carbon Nanorods as Efficient Oxygen Reduction Catalyst for Metal–Air Battery. *Nano Res.* **2023**, *16*, 8773–8781. [[CrossRef](#)]
23. Chen, J.; Ren, B.; Cui, H.; Wang, C. Constructing Pure Phase Tungsten-Based Bimetallic Carbide Nanosheet as An Efficient Bifunctional Electrocatalyst for Overall Water Splitting. *Small* **2020**, *16*, 1907556. [[CrossRef](#)] [[PubMed](#)]
24. Guo, J.; Mao, Z.; Yan, X.; Su, R.; Guan, P.; Xu, B.; Zhang, X.; Qin, G.; Pennycook, S.J. Ultrasmall Tungsten Carbide Catalysts Stabilized in Graphitic Layers for High-Performance Oxygen Reduction Reaction. *Nano Energy* **2016**, *28*, 261–268. [[CrossRef](#)]
25. Garca-A-Romeral, N.; Morales-Garca, . A.; Vines, F.; De PR Moreira, I.; Illas, F. The Nature of The Electronic Ground State of M<sub>2</sub>C (M= Ti, V, Cr, Zr, Nb, Mo, Hf, Ta, And W) Mxenes. *Phys. Chem. Chem. Phys.* **2023**, *25*, 31153–31164. [[CrossRef](#)]
26. Qin, T.; Wang, Z.; Wang, Y.; Besenbacher, F.; Otyepka, M.; Dong, M. Recent Progress in Emerging Two-Dimensional Transition Metal Carbides. *Nano-Micro Lett.* **2021**, *13*, 183. [[CrossRef](#)] [[PubMed](#)]
27. Wang, J.; Bai, L.; Yao, C.; Niu, L. A DFT Computational Prediction of 2H Phase W<sub>2</sub>C Monolayer and the Effect of O Functional Groups. *Phys. Lett. A* **2022**, *424*, 127842. [[CrossRef](#)]
28. Chen, X.; Liu, Q.; Zhang, H.; Zhao, X. Exploring High-Efficiency Electrocatalysts of Metal-Doped Two-Dimensional C<sub>4</sub>N for Oxygen Reduction, Oxygen Evolution, and Hydrogen Evolution Reactions by First-Principles Screening. *Phys. Chem. Chem. Phys.* **2022**, *24*, 26061–26069. [[CrossRef](#)]
29. Hu, H.; Zhang, P.; Xiao, B.-B.; Mi, J.-L. Theoretical Study of P-Block Metal–Nitrogen–Carbon Single-Atom Catalysts for the Oxygen Reduction Reaction. *Catal. Sci. Technol.* **2022**, *12*, 6751–6760. [[CrossRef](#)]
30. Jing, T.; Liang, D.; Deng, M.; Cai, S.; Qi, X. Density Functional Theory Studies of Heteroatom-Doped Graphene-Like Gan Monolayers as Electrocatalysts for Oxygen Evolution and Reduction. *ACS Appl. Nano Mater.* **2021**, *4*, 7125–7133. [[CrossRef](#)]
31. Gouveia, J.D.; Morales-Garcia, A.; Vines, F.; Gomes, J.R.; Illas, F. Facile Heterogeneously Catalyzed Nitrogen Fixation by Mxenes. *ACS Catal.* **2020**, *10*, 5049–5056. [[CrossRef](#)]
32. Glechner, T.; Tomastik, C.; Badisch, E.; Polcik, P.; Riedl, H. Influence of WC/C Target Composition and Bias Potential on the Structure-Mechanical Properties of Non-Reactively Sputtered WC Coatings. *Surf. Coat. Technol.* **2022**, *432*, 128036. [[CrossRef](#)]
33. Grimme, S.; Antony, J.; Ehrlich, S.; Krieg, H. A Consistent and Accurate Ab Initio Parametrization of Density Functional Dispersion Correction (DFT-D) for the 94 Elements H–Pu. *J. Chem. Phys.* **2010**, *132*, 154104. [[CrossRef](#)] [[PubMed](#)]
34. Gouveia, J.D.; Vines, F.; Illas, F.; Gomes, J.R. Mxenes Atomic Layer Stacking Phase Transitions and their Chemical Activity Consequences. *Phys. Rev. Mater.* **2020**, *4*, 054003. [[CrossRef](#)]
35. Monkhorst, H.J.; Pack, J.D. Special Points for Brillouin-Zone Integrations. *Phys. Rev. B* **1976**, *13*, 5188. [[CrossRef](#)]
36. Xiao, B.; Yang, L.; Liu, H.; Jiang, X.; Aleksandr, B.; Song, E.; Jiang, Q. Designing Fluorographene with Fen<sub>4</sub> and Con<sub>4</sub> Moieties for Oxygen Electrode Reaction: A Density Functional Theory Study. *Appl. Surf. Sci.* **2021**, *537*, 147846. [[CrossRef](#)]
37. Halgren, T.A.; Lipscomb, W.N. The Synchronous-Transit Method for Determining Reaction Pathways and Locating Molecular Transition States. *Chem. Phys. Lett.* **1977**, *49*, 225–232. [[CrossRef](#)]
38. Lin, L.; Yang, X.; Shi, P.; Yan, L.; Xie, K.; Deng, C.; Chen, Z. Probing the Origin of Transition Metal Carbide VC for Oxygen Reduction Reaction: A DFT Study. *Surf. Interfaces* **2023**, *40*, 103100. [[CrossRef](#)]
39. Radin, M.D.; Rodriguez, J.F.; Tian, F.; Siegel, D.J. Lithium Peroxide Surfaces are Metallic, while Lithium Oxide Surfaces are Not. *J. Am. Chem. Soc.* **2012**, *134*, 1093–1103. [[CrossRef](#)]
40. Yang, Y.; Wang, Y.; Yao, M.; Wang, X.; Huang, H. First-Principles Study of Rocksalt Early Transition-Metal Carbides as Potential Catalysts for Li–O<sub>2</sub> Batteries. *Phys. Chem. Chem. Phys.* **2018**, *20*, 30231–30238. [[CrossRef](#)]
41. Zhao, L.; Feng, J.; Abbas, A.; Wang, C.; Wang, H. MOF-Derived Mn<sub>2</sub>O<sub>3</sub> Nanocage with Oxygen Vacancies as Efficient Cathode Catalysts for Li–O<sub>2</sub> Batteries. *Small* **2023**, *19*, 2302953. [[CrossRef](#)] [[PubMed](#)]

42. Li, J.; Shu, C.; Liu, C.; Chen, X.; Hu, A.; Long, J. Rationalizing the Effect of Oxygen Vacancy on Oxygen Electrocatalysis in Li–O<sub>2</sub> Battery. *Small* **2020**, *16*, 2001812. [[CrossRef](#)] [[PubMed](#)]
43. Hummelshøj, J.; Luntz, A.C.; Nørskov, J. Theoretical Evidence for Low Kinetic Overpotentials in Li–O<sub>2</sub> Electrochemistry. *J. Chem. Phys.* **2013**, *138*, 034703. [[CrossRef](#)] [[PubMed](#)]
44. Yang, Y.; Xue, X.; Qin, Y.; Wang, X.; Yao, M.; Qin, Z.; Huang, H. Oxygen Evolution Reaction on Pristine and Oxidized Tic (100) Surface in Li–O<sub>2</sub> Battery. *J. Phys. Chem. C* **2018**, *122*, 12665–12672. [[CrossRef](#)]
45. Ding, S.; Wu, L.; Yuan, X. Regulating D-Orbital Electronic Configuration of Ni-Based Chalcogenides to Enhance the Oxygen Electrode Reactions in Li–O<sub>2</sub> Batteries. *Chem. Eng. J.* **2023**, *478*, 147473. [[CrossRef](#)]
46. Lian, Z.; Lu, Y.; Zhao, S.; Li, Z.; Liu, Q. Engineering the Electronic Interaction Between Atomically Dispersed Fe and RuO<sub>2</sub> Attaining High Catalytic Activity and Durability Catalyst for Li–O<sub>2</sub> Battery. *Adv. Sci.* **2023**, *10*, 2205975. [[CrossRef](#)] [[PubMed](#)]
47. Zheng, X.; Yuan, M.; Zhao, Y.; Li, Z.; Shi, K.; Li, H.; Sun, G. Status and Prospects of Mxene-Based Lithium–Oxygen Batteries: Theoretical Prediction and Experimental Modulation. *Adv. Energy Mater.* **2023**, *13*, 2204019. [[CrossRef](#)]
48. Bashir, T.; Ismail, S.A.; Wang, J.; Zhu, W.; Zhao, J.; Gao, L. Mxene Terminating Groups O–F Or–OH–F Or O–OH–F, or O–OH–Cl? *J. Energy Chem.* **2023**, *76*, 90–104. [[CrossRef](#)]
49. Wang, J.; Xu, J.; Li, B.; Lin, M.; Wang, T.; Zhen, Y.; Huang, Z.; Xing, W.; Zhao, L. Theoretical Study of Catalytic Performance of WN Mxenes as Cathodes for Li–O<sub>2</sub> Batteries: Effects of Surface Functionalization and Atomic Layers. *Appl. Surf. Sci.* **2023**, *638*, 158027. [[CrossRef](#)]
50. Bai, X.; Guan, J. Applications of Mxene-Based Single-Atom Catalysts. *Small Struct.* **2023**, *4*, 2200354. [[CrossRef](#)]
51. Tian, G.; Xu, H.; Wang, X.; Wen, X.; Zeng, T.; Liu, S.; Fan, F.; Xiang, W.; Shu, C. Optimizing D-Orbital Occupation on Interfacial Transition Metal Sites via Heterogeneous Interface Engineering to Accelerate Oxygen Electrode Reaction Kinetics in Lithium–Oxygen Batteries. *Nano Energy* **2023**, *117*, 108863. [[CrossRef](#)]
52. Tereshchuk, P.; Golodnitsky, D.; Natan, A. Trends in the Adsorption of Oxygen and Li<sub>2</sub>O<sub>2</sub> on Transition-Metal Carbide Surfaces: A Theoretical Study. *J. Phys. Chem. C* **2020**, *124*, 7716–7724. [[CrossRef](#)]
53. Jiang, Z.; Wen, B.; Huang, Y.; Guo, Y.; Wang, Y.; Li, F. New Reaction Pathway of Superoxide Disproportionation Induced by a Soluble Catalyst in Li–O<sub>2</sub> Batteries. *Angew. Chem.* **2024**, *136*, E202315314. [[CrossRef](#)]
54. Zheng, J.; Zhang, W.; Wang, R.; Wang, J.; Zhai, Y.; Liu, X. Single-Atom Pd–N<sub>4</sub> Catalysis for Stable Low-Overpotential Lithium–Oxygen Battery. *Small* **2023**, *19*, 2204559. [[CrossRef](#)] [[PubMed](#)]
55. Zheng, L.J.; Song, L.N.; Wang, X.X.; Liang, S.; Wang, H.F.; Du, X.Y.; Xu, J.J. Intrinsic Stress-Strain in Barium Titanate Piezocatalysts Enabling Lithium–Oxygen Batteries with Low Overpotential and Long Life. *Angew. Chem. Int. Ed.* **2023**, *62*, E202311739. [[CrossRef](#)] [[PubMed](#)]
56. Ding, Y.; Huang, Y.; Li, Y.; Zhang, T.; Wu, Z.S. Regulating Surface Electron Structure of PtNi Nanoalloy Via Boron Doping for High-Current-Density Li–O<sub>2</sub> Batteries with Low Overpotential and Long-Life Cyclability. *Smartmat* **2024**, *5*, E1150. [[CrossRef](#)]
57. Li, G.; Li, N.; Peng, S.; He, B.; Wang, J.; Du, Y.; Zhang, W.; Han, K.; Dang, F. Highly Efficient Nb<sub>2</sub>C Mxene Cathode Catalyst with Uniform O-Terminated Surface for Lithium–Oxygen Batteries. *Adv. Energy Mater.* **2021**, *11*, 2002721. [[CrossRef](#)]
58. Wang, L.; Lu, Y.; Xie, M.; Zhao, S.; Li, Z.; Liu, Q. Interfacially Engineered Induced Nickel-Based Heterostructures as Efficient Catalysts for Li–O<sub>2</sub> Batteries. *Electrochim. Acta* **2023**, *437*, 141476. [[CrossRef](#)]
59. Zhao, D.; Wang, P.; Di, H.; Zhang, P.; Hui, X.; Yin, L. Single Semi-Metallic Selenium Atoms on Ti<sub>3</sub>C<sub>2</sub> Mxene Nanosheets as Excellent Cathode for Lithium–Oxygen Batteries. *Adv. Funct. Mater.* **2021**, *31*, 2010544. [[CrossRef](#)]
60. Tian, G.; Ren, L.; Xu, H.; Zeng, T.; Wang, X.; Wen, X.; Du, D.; Yan, Y.; Liu, S.; Shu, C. Metal Sulfide Heterojunction with Tunable Interfacial Electronic Structure as An Efficient Catalyst for Lithium–Oxygen Batteries. *Sci. China Mater.* **2023**, *66*, 1341–1351. [[CrossRef](#)]
61. Ding, S.; Wu, L.; Zhang, F.; Yuan, X. Modulating Electronic Structure with Copper Doping to Promote the Electrocatalytic Performance of Cobalt Disulfide in Li–O<sub>2</sub> Batteries. *Small* **2023**, *19*, 2300602. [[CrossRef](#)]
62. Feng, J.; Wang, H.; Guo, L.; Su, W.; Zhao, L.; Li, G.; Chen, T.; Wang, C.; Dang, F. Stacking Surface Derived Catalytic Capability and By-Product Prevention for High Efficient Two Dimensional Bi<sub>2</sub>Te<sub>3</sub> Cathode Catalyst in Li–Oxygen Batteries. *Appl. Catal. B Environ.* **2022**, *318*, 121844. [[CrossRef](#)]
63. Jiang, H.; Zhao, T.; Shi, L.; Tan, P.; An, L. First-Principles Study of Nitrogen-, Boron-Doped Graphene and Co-Doped Graphene as the Potential Catalysts in Nonaqueous Li–O<sub>2</sub> Batteries. *J. Phys. Chem. C* **2016**, *120*, 6612–6618. [[CrossRef](#)]

**Disclaimer/Publisher’s Note:** The statements, opinions and data contained in all publications are solely those of the individual author(s) and contributor(s) and not of MDPI and/or the editor(s). MDPI and/or the editor(s) disclaim responsibility for any injury to people or property resulting from any ideas, methods, instructions or products referred to in the content.